catalysts

MDPI

Article

Optical Management of CQD/AgNP@SiNW Arrays with Highly Efficient Capability of Dye Degradation

Po-Hsuan Hsiao [1], Sasimontra Timjan [1], Kuan-Yi Kuo [1], Joon-Ching Juan [2] and Chia-Yun Chen [1,3,*]

[1] Department of Materials Science and Engineering, National Cheng Kung University, Tainan 70101, Taiwan; k811207416@gmail.com (P.-H.H.); sasimontra06@gmail.com (S.T.); kuanyi1115@gmail.com (K.-Y.K.)
[2] Nanotechnology & Catalysis Research Centre, Institute for Advanced Studies, University of Malaya, Kuala Lumpur 50603, Malaysia; jcjuan@um.edu.my
[3] Hierarchical Green-Energy Materials (Hi-GEM) Research Center, National Cheng Kung University, Tainan 70101, Taiwan
* Correspondence: timcychen@mail.ncku.edu.tw; Tel.: +886-6-275-7575 (ext. 62952)

Abstract: The facile synthetic method for the preparation of incorporated carbon quantum dots (CQDs)/Ag nanoparticles (AgNPs) with well-aligned silicon nanowire (SiNW) arrays is demonstrated, offering the superior photodegradation capabilities covering UV to visible wavelength regions. By examining the morphology, microstructure, crystallinity, chemical feature, surface groups, light-emitting, and reflection characteristics, these hybrid heterostructures are systematically identified. Moreover, the involving degradation kinetics, band diagram, cycling capability, and underlying mechanism of photodegradation are investigated, validating their remarkable and reliable photocatalytic performances contributed from the strongly reduced light reflectivity, superior capability of charge separation, and sound wettability with dye solutions.

Keywords: carbon nanodots; silicon nanowires; heterostructure; photodegradation

Citation: Hsiao, P.-H.; Timjan, S.; Kuo, K.-Y.; Juan, J.-C.; Chen, C.-Y. Optical Management of CQD/AgNP@SiNW Arrays with Highly Efficient Capability of Dye Degradation. *Catalysts* **2021**, *11*, 399. https://doi.org/10.3390/catal11030399

Academic Editor: Vincenzo Vaiano

Received: 24 February 2021
Accepted: 18 March 2021
Published: 22 March 2021

1. Introduction

Heterostructures, through the incorporation of distinct semiconductor and/or metal nanostructures, have emerged as the extensive investigations arisen from their innovative and superior optoelectronic [1,2], mechanic [3], and optical [4–7] properties, which further lead to the substantial improvement of various applications, ranging from photodetectors [8–11], solar cells [12–14], optical communications [15], to biological detection [16]. In the practical regard, nevertheless, the synthetic method of heterostructures turn out to be critical for attaining the requirement of manufacturing standards such as large production, simple procedure and sound reliability. Compared with the reported methods including chemical vapor deposition, physical evaporation, laser-induced deposition, hydrothermal, and in-situ nanoparticle synthesis [17–21], solution-processing techniques allow several superiorities, such as simple, inexpensive, and large-quantitative production of nanosized heterostructures [22], which are highly potential for addressing practical employment of commercial product. Yet, the correlated studies are still limited so far.

In this study, all-solution based method is presented for the preparation of highly efficient photocatalysts through the strategy of heterostructure design. Organic dyes, one of the dominant water pollutants, cause the serious destruction to the ecosystems. Degradation of organic dyes using photocatalysts under light illuminations has been considered the efficient and reliable treatment that can ecofriendly degrade the harmful dyes to CO_2 and water. To realize the broadband photocatalysts that can activate the dye degradation covering the wide spectral regions from ultraviolet (UV) to visible illuminations, optical management of heterostructures for accomplishing the efficient light absorption of both UV and visible wavelengths turns out to be critically essential. Herein, the well incorporation of Ag nanoparticles (AgNPs) as outer sides with carbon nanodots (CQDs)

as inner cores functioning as the broadband absorbers is demonstrated, where the AgNP shells enable to absorb the visible lights centered as 410 nm due to the existence of localized surface plasmon resonance, and the CQD shells essentially facilitate the remarkable light absorption at UV regions. In addition, the as-synthesized hybrid CQD/AgNP nanostructures are uniformly decorated on Si nanowire (SiNW) arrays. Such regulated features allow the well separation of CQD/AgNP nanoparticles rather than the unwanted aggregation, which supports the tailored absorption of broadband incoming lights for sustaining the photodegradation of organic dyes in efficient and reliable way. Moreover, the involved degradation kinetics, cycling capability, and underlying mechanism are investigated thoroughly.

2. Results and Discussion

Figure 1a presents the schematic illustration for the formation of AgNP-incorporated CQDs. Briefly, a solution phase containing glucose as carbon precursor is subjected to a sonication treatment, where the cavitation is introduced in the aqueous medium and followed by the creation of substantial strain rate due to the collapse of vapor cavities. Such involved shear stress is relatively high, thus enabling to separate the glucose molecules into few segments and in turn driving the heterogeneous formation of numerous carbon clusters with irregular shapes suspended in the solutions. Next, the subsequent supplement of heat treatment forces the rearrangement of the separated carbon clusters, which results in the formation of sphere-like quantum dots that is energetically driven by the reduction of surface energy of carbon nanostructures. It should be noted that the generated CQDs through ultrasound-driven mechanical vibrations possess the sound water solubility due to the existence of -OH groups and -CO groups on CQD surfaces, which will be evidenced ater.

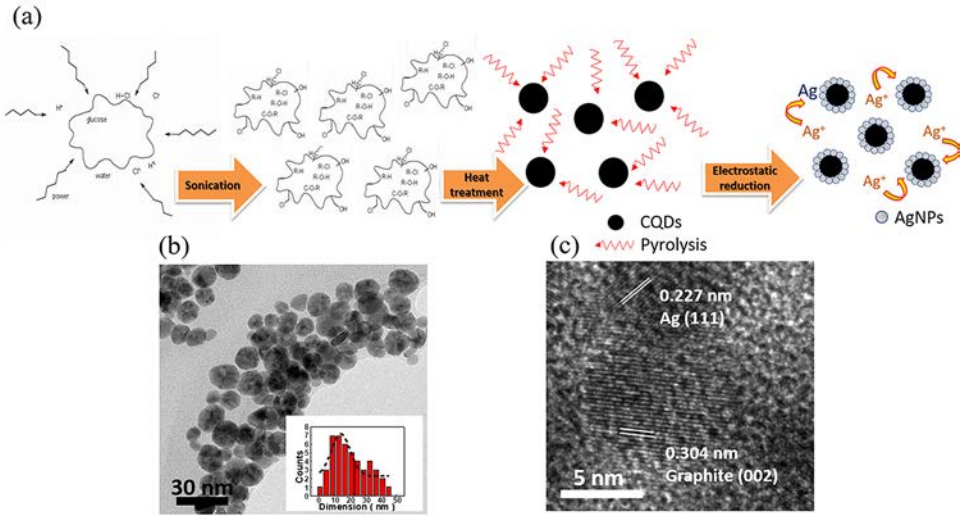

Figure 1. (**a**) Schematic illustrations for the formantion of CQD/AgNP nanoparticles. (**b**) Correlated TEM image and (**c**) HRTEM image of CQD/AgNP nanoparticles. The inset of Figure 1b presents the particle distribution with Gaussian fitting.

For synthesizing AgNP-decorated CQDs functioning as broadband absorption probes, the cationic $Ag(NH_3)^{2+}$ ion was introduced in the CQD-contained solutions, which are preferentially reacted with O-H groups on CQD surfaces due to strong electrostatic attraction, and in turn initiate the reduction of Ag clusters following the reaction presented as below [23],

$$2HR\text{-}C{=}O + 2Ag^{+} + 2OH^{-} \rightarrow 2HR\text{-}COOH + 2Ag + 2H_2O \quad (1)$$

where R represents the CQDs. Specifically, the adhered $Ag(NH_3)^{2+}$ molecules on CQD surfaces are rapidly reduced to Ag as long as the -OH groups of CQDs are exposed to the Ag+ containing solutions. Thus, the oxidation and reduction reactions are ceased while the AgNPs are fully surrounded CQDs rather than directly formed in the solutions, which guarantees the well incorporation of AgNP shells with CQD cores. In addition,

Figure 1b demonstrates the TEM image of the synthesized CQD/AgNP nanoparticles, where the sizes are uniform with the average dimension of 14.5 nm extracted from Gaussian fitting. The corresponding microstructures can be further examined, indicating the existence of Ag (111) crystallographic planes at side region of observed nanoparticles, along with graphite lattice with orientated plane of (002) locating at inner region of nanoparticles. This finding implies the successful formation of hybrid CQD/AgNP structures.

The obtained CQD/AgNP nanoparticles are then readily deposited on the sidewalls of SiNW arrays via a facile drop coating method (Figure 2a) and the corresponding EDS spectrum is also presented in the inset of Figure 2a, indicating the sound incorporation of CQD/AgNP nanoparticles with SiNW arrays. These features with highly dense decoration of functional CQD/AgNP nanoparticles are realized with standard drop coating route, which are reliable for the preparation of these hybrid heterostructures with high yield. Moreover, the SiNWs not only behave as supporting skeleton for preventing from particle aggregation of CQD/AgNP during photocatalytic operation, but further facilitate the charge separation of photogenerated carriers excited with the light illuminations. To further examine the lattice crystallinity of synthesized samples, XRD investigations are performed, as shown in Figure 2b. The correlated diffraction spectra of samples including SiNWs, CQD@SiNWs and CQD/AgNP@SiNWs are examined, indicating that the consistent peaks located at 61.6° and 69.2° are corresponded to Si (320) and Si (400) crystallographic planes, respectively [24]. Moreover, one can also observe the explicit peak located at 25.6° from both cases of CQDs and CQD/AgNP, which arises from the crystallite configuration of graphite (002) lattice [25]. It should be noted that compared with conventional diffraction patterns of graphite, the slightly small diffraction angle is attributed to the O-H functional groups at the edges of CQD structures that expand the graphite lattice of CQDs. In hybrid features of CQD/AgNP@SiNWs, several additional diffraction peaks at 38.1°, 44.3°, 64.4° and 77.3° are exhibited, which indicate the (111), (200) and (311) of FCC configurations from Ag crystals, respectively [26,27]. In addition, the grain size of sole CQDs and CQD/AgNP structures are estimated using Scherrer's formula. The results evidence that the grain sizes of CQD/AgNP structures are 0.45 nm (CQDs) and 14.57 nm (AgNPs), where the former one is comparably smaller than that of sole CQDs (0.61 nm) due to the fact that the crystallite CQDs are surrounded by Ag shells, indicating the successful formation of core/shell features, and these findings are correlated with TEM investigations, as shown in Figure 1c.

To further examine the distinct crystallographic configuration of hybrid CQD/AgNP@SiNWs while the heterojunction between CQD nanoparticles and underlying Si skeletons is established, Raman analysis is performed, and the recorded spectra are demonstrated in Figure 2c. Interestingly, it can be found that the Raman peak at 925 cm^{-1} originally from Si-O vibrations of Si crystals is solely presented in the sample of pure SiNWs, but turns out to disappear while the CQDs or CQD/AgNPs are involved. This explicitly finding implies the fact that the Si-O bonding of Si surfaces in contact with CQDs is reduced, thus leaving the establishment of CQD/Si heterojunction that can substantially benefit the charge rectification of photogenerated carriers across CQD/Si interfaces. Moreover, the appearance of characteristic Raman peaks of D band (1371 cm^{-1}) and G band (1570 cm^{-1}) of graphite crystals can be found in CQD@SiNWs [28,29], whereas the slight blueshift of D band (1368 cm^{-1}) appearing in the sample of CQD/AgNP@SiNWs is exhibited, which could be attributed to the electrostatic attraction bridged between AgNPs and CQDs, where this result is corresponded with the literature [30]. In addition, Figure 2d demonstrates the XPS spectrum for the identification of chemical state of hybrid CQD/AgNP@SiNWs, where the intense XPS peaks locate at 368.6 and 374.6 eV are corresponded to the $3d^{5/2}$ and $3d^{3/2}$ of Ag signals, indicating the existence of metallic state of Ag that can effectively absorb visible lights for photocatalytic use operated in visible regions.

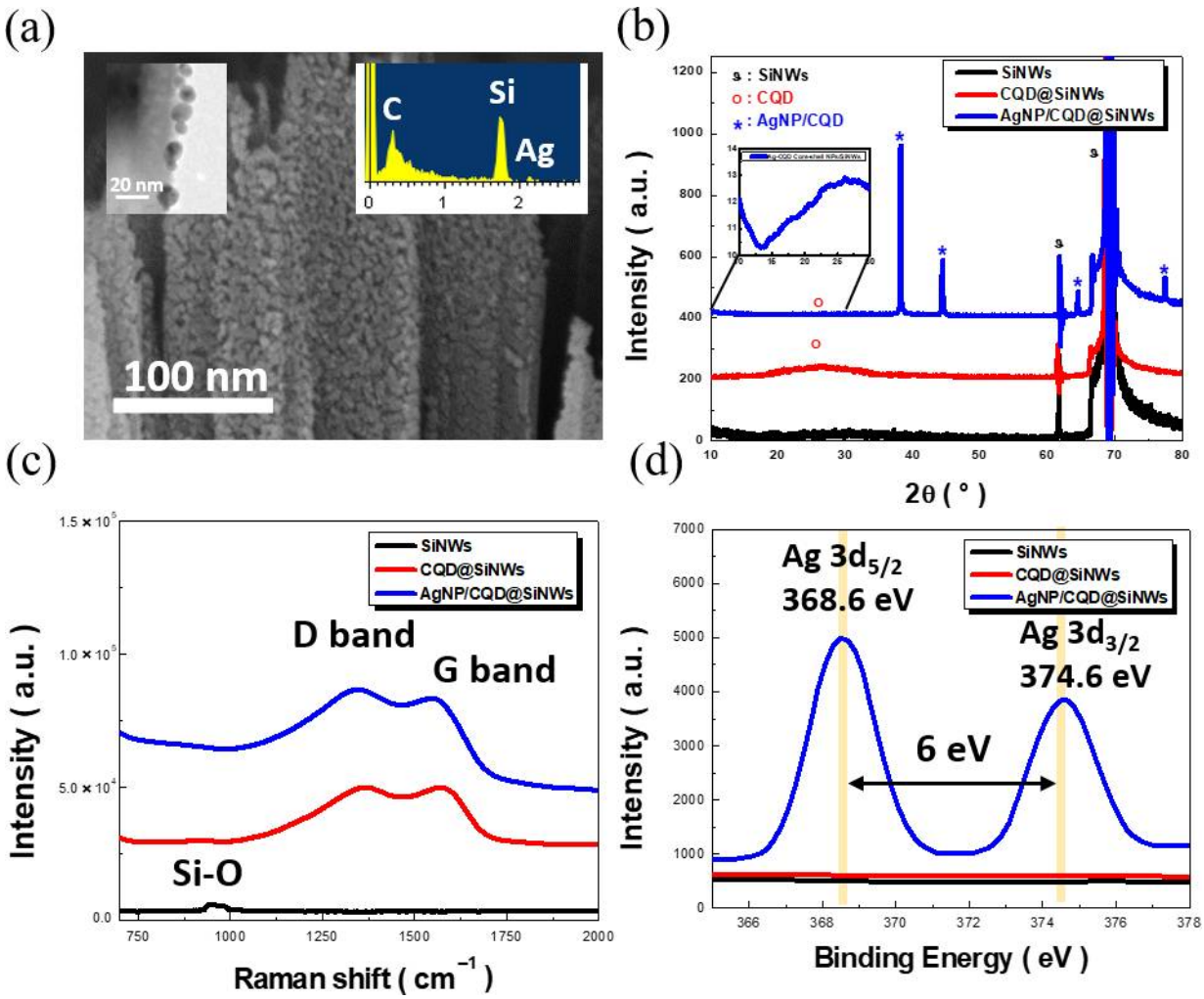

Figure 2. (**a**) Cross-sectional SEM image of CQD/AgNP@SiNW arrays. The inset of Figure 2a shows the corresponding TEM image (figure **left**) and EDS spectrum (figure **right**), respectively. (**b**) XRD and (**c**) Raman analysis of three various samples. (**d**) XPS investigations of SiNW, CQD@SiNW and CQD/AgNP@SiNW arrays, respectively.

Figure 3a demonstrates the FTIR spectra of three various SiNW-based samples. Compared with the spectrum of sole SiNWs, one can observe several absorption dips including 2900 cm^{-1}, 1735 cm^{-1}, 1600 cm^{-1}, 1380 cm^{-1}, 1035 cm^{-1}, and 635 cm^{-1} from both CQD@SiNWs and CQD/AgNP@SiNWs, which are contributed from stretching vibrations of CH_3, C=O, C=C, nitrate, C-O and CH_2 bonding, respectively. The existence of nitrate band is mainly attributed to the residual $Ag(NH_3)^{2+}$ ions absorbed on the surfaces of AgNPs. These strongly correlated FTIR features from CQD@SiNWs and CQD/AgNP@SiNWs indicate that the decoration of AgNPs does not alter the chemical structures of CQDs, while the solution-processing technique presented here may offer an effective route for realizing the well optical management of such hybrid nanostructures for attaining broadband absorption of light.

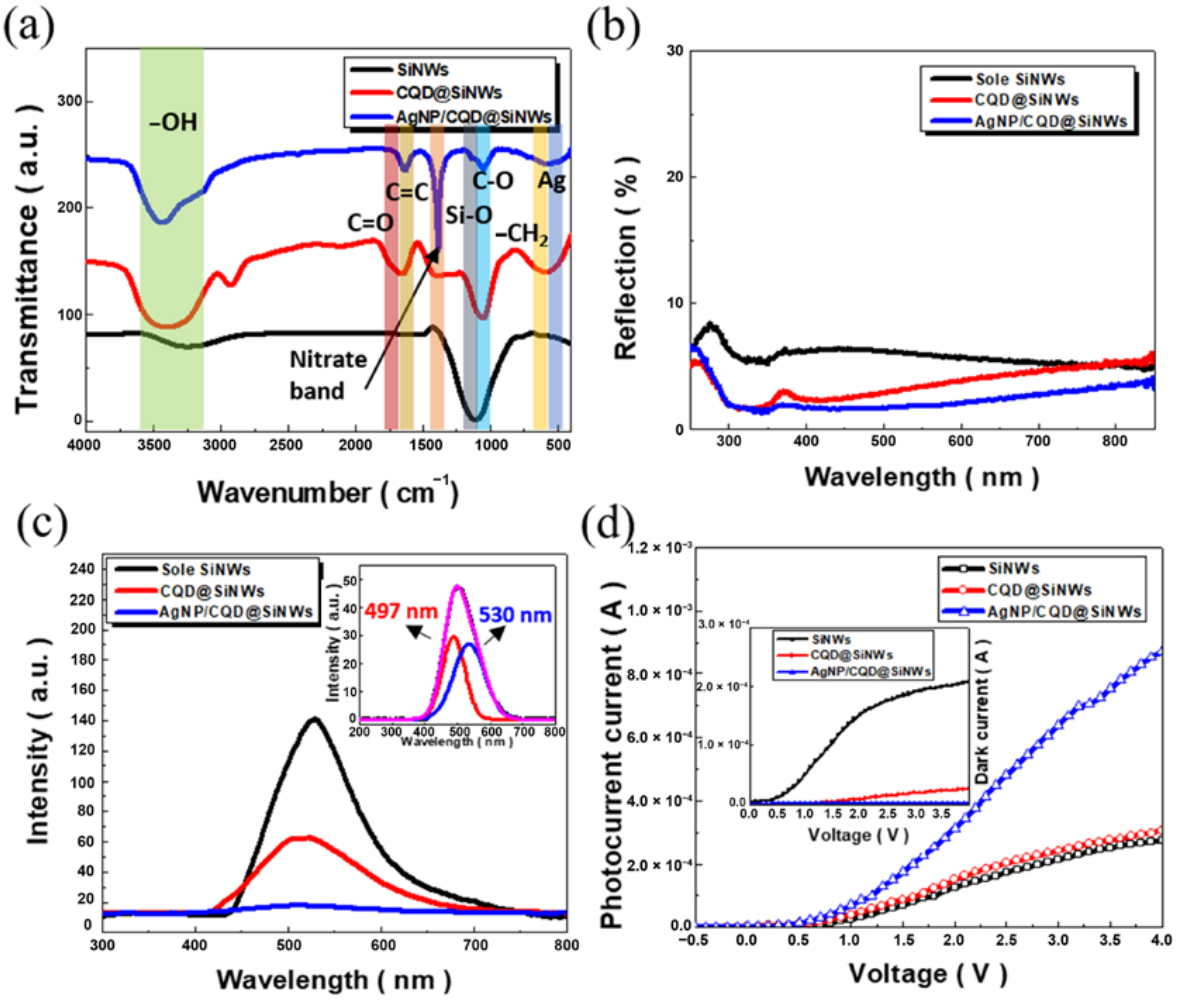

Figure 3. (**a**) FTIR, (**b**) light-reflectivity and (**c**) PL spctra of three various samples. (**d**) Measured results of photocurrent and dark current (inset of Figure 3d) of three various samples.

In addition, the correlated light reflectivity from sample surfaces acts as the deceive role on determining the interaction of incoming lights with photocatalysts, and therefore the well management of light absorption turns out to be significant for the extent of photodegradation performances. Here, the light reflectivity covering the wavelengths from 250 to 850 nm of three various SiNW-based samples are examined, as shown in Figure 3b. All three samples demonstrate the low reflectivity over the broadband spectra regions, with average reflectivity of 6.63% from sole SiNWs, 3.86% from CQD/SiNWs and 2.21% from CQD/AgNP@SiNWs. The ultra-low light reflectivity existed in CQD/AgNP@SiNWs can be attributed to two possible effects. First, the involved CQDs own the excellent light absorption in UV regions, where the dominant absorption bands covered around 200–300 nm stemming from π-π^* transition of C=C bonding, and another absorption region centered at 230 nm is originated from the n-π^* transition of C=O bonding [31]. Secondly, the hybrid CQD/AgNP nanostructures can additionally offer the strong visible-light absorption centered at 410 nm coming from the effect of localized surface plasmonic resonance (LSPR) of metallic Ag, where the incoming lights are strongly absorbed within AgNPs due to the collective oscillation of electrons [16]. These combined effects thus greatly reduce the average light reflectivity of CQD/AgNP@SiNWs approximately three times compared with sole SiNWs, further extending the absorption range covering from UV to visible regions, which facilitate the possible photodegradation process under broadband illuminations.

The light-emitting characteristics of three various SiNW-based photocatalysts are explored. In sole SiNWs, the dominant PL peak can be found in 530 nm, which is orig-

inated from the radiative emission of S-O bonding of SiO_x crystals [32]. When incorporating SiNWs with CQD nanoparticles, the combined PL signals exist, which can be deconvoluted into two characteristic peaks at 530 nm and 497 nm, as shown in Figure 3c. Specifically, the PL spectral position centered at 497 nm is assigned to be the fundamental emission of CQD structures, which are in line with the literature [33]. Moreover, one can obtain the obvious reduction of PL intensities, which implies the possible separation of photoexcited carriers, rather than experiencing the radiative recombination due to the creation of sound heterojunction between the decorated CQDs and supported SiNWs. Moreover, when the CQD/AgNP@SiNWs heterostructures are realized, the PL emission is almost ceased. Such PL quenching feature can be interpreted by the fact that the photogenerated holes from CQDs can separately transport to AgNPs, whereas the photoexcited electrons are driven to SiNW sides, and thus the carriers can be effectively separated, promoting the use of both photo-created electrons and holes for the activation of dye degradation. To further support these findings, the excited currents of samples under the sweeping bias from -0.5 to 4.0 V in the presence of either illuminations of 405-nm light or dark condition are evaluated, where the former correlates with the creation of photocurrents, and the latter involves with the excitation of dark currents, as shown in Figure 3d. The measured photocurrents at 4.0 V under light illuminations are found to be 2.75×10^{-4} A (SiNWs), 3.06×10^{-4} A (CQD@SiNWs) and 8.71×10^{-4} A (CQD/AgNP@SiNWs), where the origin of leading photocurrent performance from CQD/AgNP@SiNWs can be contributed from the strongly reduced light reflectivity and superior capability of charge separation, as evidenced in Figure 3b,c. In addition, the extracted dark currents of CQD/AgNP@SiNWs (2.13×10^{-6} A) are the lowest in these three samples, which is two order of magnitude lower than sole SiNWs (2.07×10^{-4} A), as presented in the inset of Figure 3d. Such a feature is supported by the sound rectification performance of heterostructures that possesses the effective diode behavior for suppressing the leakage currents. In addition, no obvious hysteresis in the I-V characteristics can be found from three tested samples, as presented in Supplementary Materials.

The degradation efficiency of MB dyes, in terms of C/C_0 (%), in the presence of SiNW-based photocatalysts with variations of CQD/AgNP contents are demonstrated in Figure 4a. In sole SiNWs, the trivial photodegradation efficiency can be found, which is because the involvement of rapid charge recombination appearing in Si crystals that are capable of initiating the oxidative process for dye degradation. To overcome this issue, the incorporation CQD/AgNPs with SiNWs is found to be promising, where the greatly improved photodegradation efficiency of MB dyes is achieved. Foremost is the introduction of 20 mg of CQD/AgNP nanostructures as the optimal condition for preparing the hybrid CQD/AgNP@SiNWs, whereas the introduction of a greater amount of CQD/AgNPs (24 mg) in turn will suppress the degradation performance due to the significant aggregation of CQD/AgNPs on SiNW surfaces that may impede the illumination lights entering the photocatalysts.

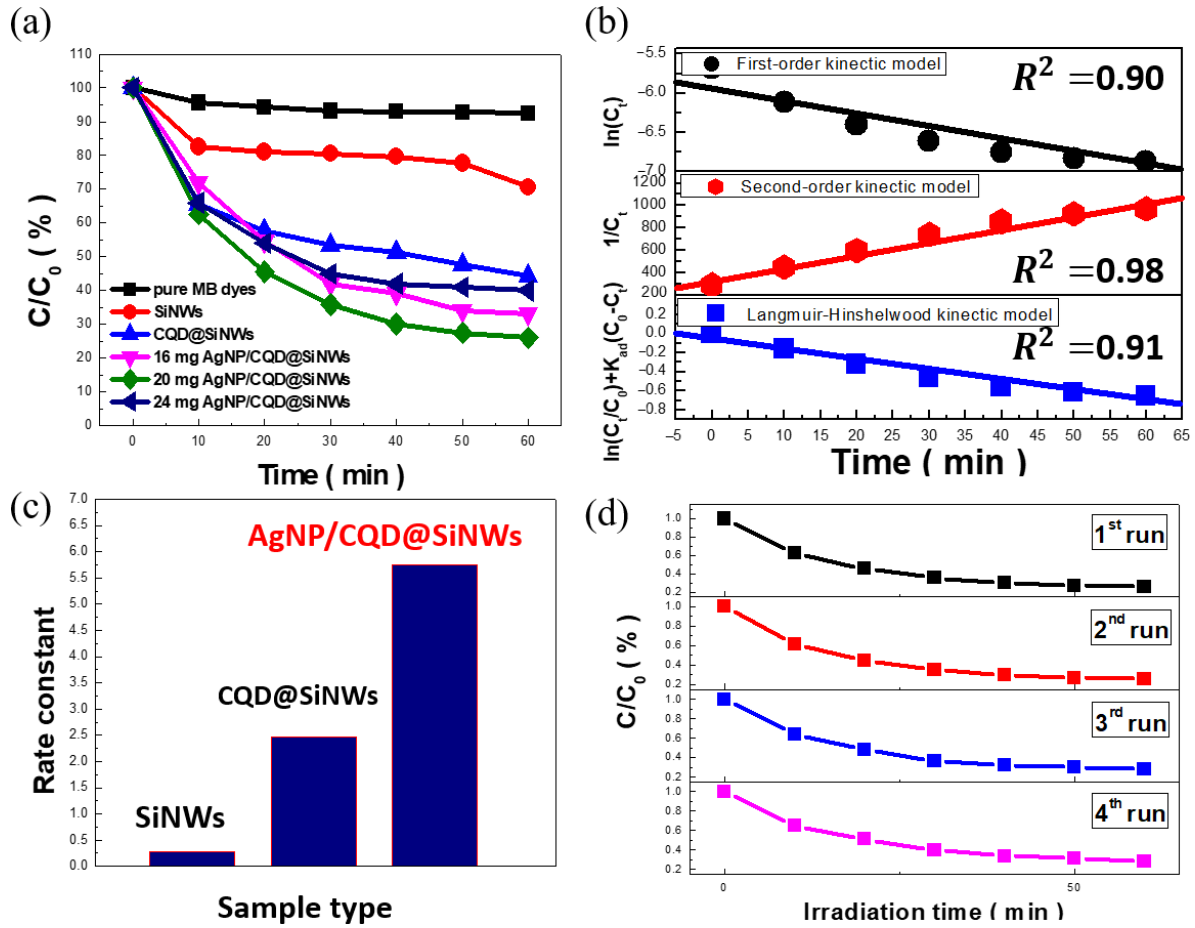

Figure 4. (**a**) Photodegradation results of MB dyes in the presence of SiNWs, CQD@SiNWs and CQD/AgNP@SiNWs with three various loading amounts of CQD/AgNP nanoparticles, respectively. (**b**) Kinetic investigations and (**c**) rate constant of MB degradation in the presence of CQD/AgNP@SiNWs (20 mg of CQD/AgNP loadings). (**d**) Cycling tests of CQD/AgNP@SiNW photocatalysts.

To model the photocatalytic kinetics, the involved reactions of dye degradation are examined with three kinetic models, including first-order kinetic model, second-order kinetic model, and Langmuir–Hinshelwood kinetic model, as expressed in the following equations.

First-order kinetic model [34]:

$$\ln C_t = -k_1 t + \ln C_0 \tag{2}$$

Second-order kinetic model [35]:

$$1/C_t = k_2 t + 1/C_0 \tag{3}$$

Langmuir-Hinshelwood kinetics model [36]:

$$\ln(C_t/C_0) + k_{ab}(C_0 - C_t) = -k_3 k_{ab} t \tag{4}$$

where C_0 and C_t are assigned as MB dyes at time = 0 and time = t, respectively. k_1, k_2 and k_3 represents the rate constants of first-order, second-order, and Langmuir-Hinshelwood, respectively. K_{ab} is assigned as the Langmuir constant. Accordingly, the fitting results from experimental investigations for three distinct kinetic models are demonstrated in Figure 4b, where the highest R_2 (0.98) appears in the second-order kinetic model, validating the underlying kinetics for dye degradation under the variations of illumination durations. Fur-

thermore, the reaction constants following the expression of second-order kinetic model are evaluated to compare the photodegrading rates of three samples, as indicated in Figure 4c. The results evidence that the rate constant of hybrid CQD/AgNP@SiNWs is more than 2.3 times and 21 times than CQD@SiNWs and sole SiNWs, respectively, behaving the superior photocatalysts for treating the MB dyes in the aqueous media. Moreover, the reliability of MB photodegradation is monitored with four sets of consecutive cycles (Figure 4d), and the almost similar decaying curves in terms of concentration of remaining dyes with respect to the illumination time are presented for these four cycles. All these examinations suggest the reliable and efficient characteristics for the removal of MB dyes based on such hybrid photocatalysts.

Aside from the evaluation of photodegradation performances, examinations of underlying photocatalytic reactions for the removal of MB dyes were carried out based on introducing several possible scavengers, including $AgNO_3$, IPA and Na_2-EDTA for selectively trapping the photogenerated electrons, hydroxyl radicals and photogenerated holes, respectively. Figure 5a presents the corresponding results along with the photodegradation curves without adding the scavengers. One can obviously find that the involvement of all three trapping molecules affect the dye degradation efficiency of CQD/AgNP@SiNWs, while the photogenerated holes and hydroxyl radicals act the dominant roles as the degradation results are substantially suppressed due to the addition of Na_2-EDTA and IPA regents, respectively. In addition, the underlying band diagram of such CQD/AgNP@SiNW heterostructures is illustrated, as shown in Figure 5b, which elucidates the possible transport routes of photogenerated carriers. The photogenerated electrons at LUMO level of CQDs excited from light illuminations irreversibly transport to the LUMO level of Si due to band bending established by the heterojunction at CQD/SiNW interfaces. Meanwhile, the photoexcited holes at HOMO level of CQDs simultaneously transport to AuNPs owing from the energy of HOMO level (CQDs) existing below the work function of AuNPs. Such charge-transfer phenomena lead to the effective charge separation obtained by the created step-like energy diagram [37,38]. On the basis of these findings, the possible mechanism contributing to the highly efficient dye-degradation performance is illustrated in Figure 5c. It clearly indicates that both the photogenerated electrons and holes allow the activation of dye degradation through distinct routes. The released electrons from SiNWs initiate the formation of superoxide ions by reacting with O_2 in the solutions, which are highly oxidative for the photodegradation of MB dyes. On the other hand, the reactive hydroxyl radicals are created due to the interaction of released holes with water in the aqueous solutions, which offer another pathway for causing the efficient route of dye degradation, where both of them enable to establish the accelerated photodegradation process with remaining dyes.

One additional reason that benefits the photodegradation performance relates with the adsorption of MB dyes on the photocatalyst surfaces, which belongs to the initial step for the succeeding photocatalytic interaction. In this regard, the surface wettability and zeta potential of three-SiNW-based samples are measured (Figure 6), and the corresponded results are summarized in Table 1. On investigating the surface wettability, the contact angle of SiNWs is found to be $59.8 \pm 0.2^{\circ}$, whereas the CQD@SiNWs possess comparably low contact angle of $10.9 \pm 0.1^{\circ}$. This can be attributed the abundant hydroxyl groups existed in CQD surfaces that improve the surface wettability, as evidenced in Figure 3a. Moreover, the substantial improvement of surface hydrophilicity can be achieved from CQD/AgNP@SiNWs with low contact angle of $2.1 \pm 0.1^{\circ}$, which can facilitate the contact of dye solutions with photocatalysts. In addition, the sound wetting characteristics of photocatalysts with dye solutions also correlate with the magnitude of zeta potential, which stands for the dominant indicator responding the dispersed stability of nanostructures in dye solutions. It can be found that the zeta potential of CQD/AgNP@SiNWs (-56.6 mV) reaches comparably relative value than both of sole SiNWs (-15.2 mV) and CQD/SiNWs (-38.1 mV), indicating that such heterostructures are highly stable to remedy the photocatalytic process. Moreover, after four cycles of photodegradation process,

CQD/AgNP@SiNWs still maintain the unchanged zeta potential (−53.9 mV), with only less than 4% of deviation compared with original case, again verifying their reliability for long-term use.

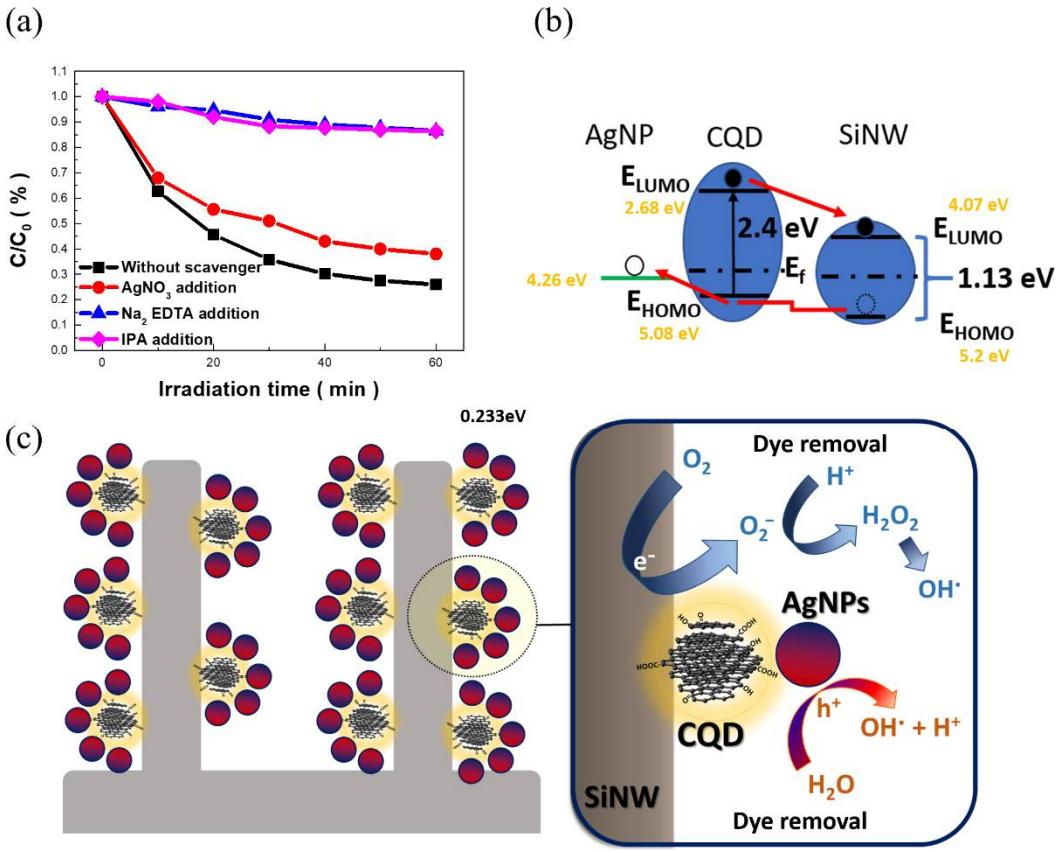

Figure 5. (**a**) Scvenger examinations of photodegradation process using CQD/AgNP@SiNWs as photocatalysts. (**b**) Correlated band diagram of hybrid heterostructures. (**c**) Possible mechanism of photodegradation of MB dyes.

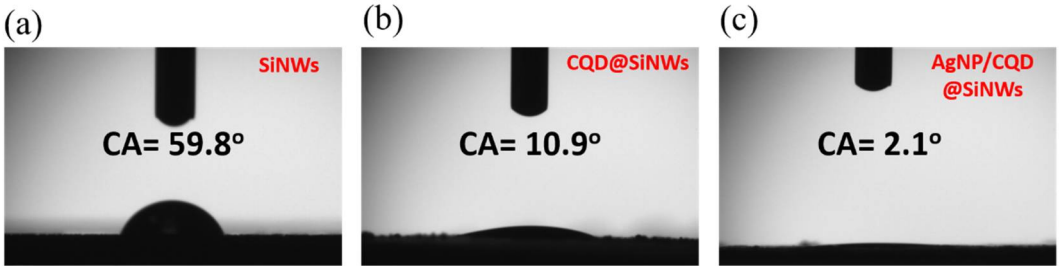

Figure 6. Contact-angle photographs of three various samples.

Table 1. Measured results of zeta potential and contact angles of various photocatalysts.

Characteristics	SiNWs	CQD/SiNWs	CQD/AgNP@SiNWs	CQD/AgNP@SiNWs (after Four-Time Photo Degradation Test)
Zeta potential (mV)	−15.2	−38.1	−56.6	−53.9
Contact angle (°)	59.8 ± 0.2	10.9 ± 0.1	2.1 ± 0.1	2.6 ± 0.2

3. Materials and Methods

3.1. Regents

Methylene blue (MB, M_w = 319.85, 100% purity), glucose (M_w = 180.16, 99% purity) and Hydrogen fluoride (HF, 48–51%) were purchased from Acros Organics. Hydrochloric acid (HCl, 37%) and nitric acid (HNO_3, 65%) were obtained from Scharlau and Panreac AppliChem, respectively. Single-crystalline Si substrates were purchased from Semiconductor Wafer Inc., Taiwan. No further purification of the regents was performed.

3.2. Formation of CQD/AgNPs

Briefly, the 2 M of HCl acid and 2 g of glucose were mixed in the gentle magnetic stir serving as precursors for the synthesis of monodispersed CQDs. The mixed solutions were sonicated with an ultrasonic vibration equipment (DC200H, oscillation frequency: 40 KHz, output: 200 W) for 4 h. Subsequently, the as-prepared solutions were annealed in the clave at 200 °C for 5 min. Finally, the as-treated samples were subjected to filter process through a 0.22 μm membrane to remove the particles which are not completed reacted. The hybrid CQD/AgNP nanostructures were synthesized by mixing the as-prepared CQDs with $AgNO_3$ under the volume ratio of 1:1 in DI water, along with introducing 32 μL of ammonium hydroxide with a concentration of 35%, and then the mixed solution was processed with the sonication treatment for 10 min. After that, the products were annealed 120 °C for 60 min

3.3. Formation of Aligned SiNWs

The single-crystalline Si substrates (Resistivity = 1–10 Ωcm) with crystallographic orientation of (100) direction with the fixed size of 1.5 cm by 1.5 cm were used as the starting materials. Prior to SiNW fabrication, the Si substrates were cleaned in the ultrasonication with acetone, isopropyl alcohol and deionized (DI) water. After that, the Si substrates were immersed the etching solutions containing 4.6 M of HF (4.6 M) and 0.01 M of $AgNO_3$ for 20 min at 25 °C for preparing SiNW arrays with vertical configuration [39–44]. Subsequently, the SiNW samples were dipped in the concentrated HNO_3 solutions (65%) to completely remove the residual silver structures. Finally, the as-prepared samples were dipped in the dilute HF solutions (1%) to etch away the grown oxide and then dried by gentle N_2 gas.

3.4. Photocatalytic Measurements

Photocatalytic degradation of methylene blue (MB dyes) were tested using a PanChum multilamp photoreactor (PR-2000) under the switchable lamp sources. In each measurement, the samples with fixed size of 1.5 cm by 1.5 cm were immersed in the dye solutions (0.2 mM, 10 mL in volume) with a constant magnetic stir. The solutions were placed in the dark condition for 1.5 h to reach the adsorption equilibrium, and then transferred to the photoreactor for initiating light-excited photocatalytic process. To measure the photodegradation result, 0.1 mL of suspension was withdrawn and the involved concentrations were characterized with a UV/visible spectrophotometer (Shimadzu UV-2401 PC).

3.5. Characterizations

Chemical structures and correlated functional groups of samples were characterized with a Fourier transform infrared (FTIR) spectra (Perkin ElmerFrontier). Morphologies and chemical composition of the prepared substrates were examined with scanning electron microscope (SEM, Hitachi S-4800) and energy dispersive spectrometer (EDS, Oxford INCA), respectively. Crystalline investigations were conducted with a Rigaku Multiflex X-ray diffractometer under Cu-K radiation. Chemical states and compositions of sample surfaces were analyzed with X-ray photoelectron spectrometer (XPS, PHI 5000 Versa Probe). Light-emitting properties of samples were characterized with a photoluminescent (PL) system equipped with light-emitting diode (LED) lamp (output power: 780 mW). UV/Vis reflection spectra were analyzed with a UV-Vis-NIR spectrophotometer (Hitachi, U3900H).

Photoelectric measurements of samples were conducted through a standard semiconductor characterization system (Keithley 2400).

4. Conclusions

Extensive investigations of incorporated CQD/AgNP nanoparticles with regular SiNW arrays made via a facile synthetic method are presented for remarkably improving the photodegradation performances of MB dyes. The low light reflectivity of 2.21%, superior capability of charge separation, and sound wettability in a highly stable form with dye solutions of these intriguing CQD/AgNP@SiNW photocatalysts are identified. By adjusting the amount of adding CQD/AgNP nanoparticles, the correlated photodegradation efficiency can be dramatically improved, and these photocatalytic features for dye removal are highly stable, showing the unchanged photodegradation behaviors for four-times cycling utilization. On the basis of such green-formation photocatalytic heterostructures, along with investigations on degradation kinetics, band structures, and mechanisms, we anticipate that this research can further pave the wat for opportunities in practical water treatment, dye detoxification, and other functional applications.

Supplementary Materials: The following are available online at https://www.mdpi.com/2073-4344/11/3/399/s1. Figure S1: Time-dependent I-V curves of sole SiNW, CQD@SiNW and CQD/AgNP@SiNW arrays. The results indicate that no obvious hysteresis in the I-V characteristics can be found; Figure S2: Light-absorption spectra of MB dyes in the presence of CQD/AgNP@SiNW arrays after experiencing light illuminations.

Author Contributions: P.-H.H., S.T. and C.-Y.C. proposed the idea and was involved in the design of experiments. P.-H.H. and K.-Y.K. performed the experimental works characterizations. P.-H.H., J.-C.J. and C.-Y.C. discussed the results and wrote the main manuscript text. All authors have read and agreed to the published version of the manuscript.

Funding: This research was funded by Ministry of Science and Technology of Taiwan (MOST 107-2221-E-006-013-MY3), and Hierarchical Green-Energy Materials (Hi-GEM) Research Center, from The Featured Areas Research Center Program within the framework of the Higher Education Sprout Project by the Ministry of Education (MOE) and the Ministry of Science and Technology (MOST 107-3017-F-006-003) in Taiwan.

Data Availability Statement: All data are shown in this manuscript.

Acknowledgments: The authors greatly thank the Instrument Center and Center for Micro/Nano Science and Technology, National Cheng Kung University with the facilities provided for conducting material characterizations.

Conflicts of Interest: The authors declare no conflict of interest.

References

1. Saenz, G.A.; Karapetrov, G.; Curtis, J.; Kaul, A.B. Ultra-high photoresponsivity in suspended metal-semiconductor-metal mesoscopic multilayer MoS_2 broadband detector from UV-to-IR with low Schottky barrier contacts. *Sci. Rep.* **2018**, *8*, 1–11. [CrossRef]
2. Li, J.; Xi, X.; Li, X.; Lin, S.; Ma, Z.; Xiu, H.; Zhao, L. Ultra-high and fast ultraviolet response photodetectors based on lateral porous gan/ag nanowires composite nanostructure. *Adv. Opt. Mater.* **2020**, *8*, 1902162. [CrossRef]
3. Liu, Y.; Li, D.; Tian, F.; Duan, D.; Liu, B.; Cui, T. Strain-engineering enables reversible semiconductor–metal transition of skutterudite IrAs 3. *Inorg. Chem. Front.* **2020**, *7*, 1108–1114. [CrossRef]
4. Hsiao, P.-H.; Wei, T.-C.; Chen, C.-Y. Stability improvement of Cu(ii)-doped ZnS/ZnO photodetectors prepared with a facile solution-processing method. *Inorg. Chem. Front.* **2021**, *8*, 311–318. [CrossRef]
5. Cesca, T.; Scian, C.; Petronijevic, E.; Leahu, G.; Voti, R.L.; Cesarini, G.; Macaluso, R.; Mosca, M.; Sibilia, C.; Mattei, G. Correlation between in situ structural and optical characterization of the semiconductor-to-metal phase transition of VO_2 thin films on sapphire. *Nanoscale* **2020**, *12*, 851–863. [CrossRef]
6. Tan, E.K.; Shrestha, P.K.; Pansare, A.V.; Chakrabarti, S.; Li, S.; Chu, D.; Lowe, C.R.; Nagarkar, A.A. Density modulation of embedded nanoparticles via spatial, temporal, and chemical control elements. *Adv. Mater.* **2019**, *31*, 1901802. [CrossRef]
7. Li, R.; Pang, C.; Li, Z.; Chen, F. Plasmonic nanoparticles in dielectrics synthesized by ion beams: Optical properties and photonic applications. *Adv. Opt. Mater.* **2020**, *8*, 1902087. [CrossRef]

8. Qin, Y.; Li, L.; Zhao, X.; Tompa, G.S.; Dong, H.; Jian, G.; He, Q.; Tan, P.; Hou, X.; Zhang, Z. Metal–semiconductor–metal ε-Ga_2O_3 solar-blind Photodetectors with a record-high responsivity rejection ratio and their gain mechanism. *ACS Photonics* **2020**, *7*, 812–820. [CrossRef]
9. Huang, C.-Y.; Lin, T.-J.; Liao, P.-C. High-performance metal-semiconductor-metal ZnSnO UV photodetector via controlling the nanocluster size. *Nanotechnology* **2020**, *31*, 495203. [CrossRef]
10. Hsiao, P.-H.; Lai, Y.-C.; Chen, C.-Y. Dual-sized carbon quantum dots enabling outstanding silicon-based photodetectors. *Appl. Surf. Sci.* **2021**, *542*, 148705. [CrossRef]
11. Chen, X.; Wang, D.; Wang, T.; Yang, Z.; Zou, X.; Wang, P.; Luo, W.; Li, Q.; Liao, L.; Hu, W. Enhanced photoresponsivity of a GaAs nanowire metal-semiconductor-metal photodetector by adjusting the fermi level. *ACS Appl. Mater. Interfaces* **2019**, *11*, 33188–33193. [CrossRef] [PubMed]
12. Yip, H.-L.; Hau, S.K.; Baek, N.S.; Jen, A.K.-Y. Self-assembled monolayer modified ZnO/metal bilayer cathodes for polymer/fullerene bulk-heterojunction solar cells. *Appl. Phys. Lett.* **2008**, *92*, 179. [CrossRef]
13. Kim, M.R.; Xu, Z.; Chen, G.; Ma, D. Semiconductor and metallic core–shell nanostructures: Synthesis and applications in solar cells and catalysis. *Chem. Eur. J.* **2014**, *20*, 11256–11275. [CrossRef]
14. Wei, T.-C.; Chen, S.-H.; Chen, C.-Y. Highly conductive PEDOT:PSS film made with ethylene-glycol addition and heated-stir treatment for enhanced photovoltaic performances. *Mater. Chem. Front.* **2020**, *4*, 3302–3309. [CrossRef]
15. Nouman, M.T.; Kim, H.-W.; Woo, J.M.; Hwang, J.H.; Kim, D.; Jang, J.-H. Terahertz modulator based on metamaterials integrated with metal-semiconductor-metal varactors. *Sci. Rep.* **2016**, *6*, 1–7.
16. Hsiao, P.-H.; Chen, C.-Y. Insights for realizing ultrasensitive colorimetric detection of glucose based on carbon/silver core/shell nanodots. *ACS Appl. Bio Mater.* **2019**, *2*, 2528–2538. [CrossRef]
17. Freedsman, J.J.; Kubo, T.; Egawa, T. Trap characterization of in-situ metal-organic chemical vapor deposition grown AlN/AlGaN/GaN metal-insulator-semiconductor heterostructures by frequency dependent conductance technique. *Appl. Phys. Lett.* **2011**, *99*, 033504. [CrossRef]
18. Li, Y.; Li, S.; He, C.; Zhu, C.; Li, Q.; Li, X.; Liu, K.; Zeng, X. Selective laser-induced preparation of metal-semiconductor nanocomposites and application for enhanced photocatalytic performance in the degradation of organic pollutants. *J. Alloys Compd.* **2021**, *867*, 159062. [CrossRef]
19. Hsiao, P.-H.; Li, T.-C.; Chen, C.-Y. ZnO/Cu_2O/Si Nanowire Arrays as Ternary Heterostructure-Based Photocatalysts with Enhanced Photodegradation Performances. *Nanoscale Res. Lett.* **2019**, *14*, 1–8. [CrossRef]
20. Pansare, A.V.; Khairkar, S.R.; Shedge, A.A.; Chhatre, S.Y.; Patil, V.R.; Nagarkar, A.A. In situ nanoparticle embedding for authentication of epoxy composites. *Adv. Mater.* **2018**, *30*, 1801523. [CrossRef]
21. Tasche, D.; Weber, M.; Mrotzek, J.; Gerhard, C.; Wieneke, S.; Möbius, W.; Höfft, O.; Viöl, W. In situ investigation of the formation kinematics of plasma-generated silver nanoparticles. *Nanomaterials* **2020**, *10*, 555. [CrossRef]
22. Tang, C.-H.; Hsiao, P.-H.; Chen, C.-Y. Efficient Photocatalysts Made by Uniform Decoration of Cu2O Nanoparticles on Si Nanowire Arrays with Low Visible Reflectivity. *Nanoscale Res. Lett.* **2018**, *13*, 1–8. [CrossRef]
23. Shen, L.; Chen, M.; Hu, L.; Chen, X.; Wang, J. Growth and stabilization of silver nanoparticles on carbon dots and sensing application. *Langmuir* **2013**, *29*, 16135–16140. [CrossRef] [PubMed]
24. Zhou, Q.; Bao, M.; Ni, X. A novel surface modification of silicon nanowires by polydopamine to prepare SiNWs/NC@ NiO electrode for high-performance supercapacitor. *Surf. Coat. Technol.* **2021**, *406*, 126660. [CrossRef]
25. Li, B.; Feng, Y.; Ding, K.; Qian, G.; Zhang, X.; Zhang, J. The effect of gamma ray irradiation on the structure of graphite and multi-walled carbon nanotubes. *Carbon* **2013**, *60*, 186–192. [CrossRef]
26. Elgamouz, A.; Idriss, H.; Nassab, C.; Bihi, A.; Bajou, K.; Hasan, K.; Abu Haija, M.; Patole, S.P. Green synthesis, characterization, antimicrobial, anti-cancer, and optimization of colorimetric sensing of hydrogen peroxide of algae extract capped silver nanoparticles. *Nanomaterials* **2020**, *10*, 1861. [CrossRef]
27. Liu, X.; Chen, J.; Yuan, J.; Li, Y.; Li, J.; Zhou, S.; Yao, C.; Liao, L.; Zhuang, S.; Zhao, Y. A silver nanocluster containing interstitial sulfur and unprecedented chemical bonds. *Angew. Chem. Int. Ed. Engl.* **2018**, *57*, 11273–11277. [CrossRef]
28. Guizani, C.; Haddad, K.; Limousy, L.; Jeguirim, M. New insights on the structural evolution of biomass char upon pyrolysis as revealed by the Raman spectroscopy and elemental analysis. *Carbon* **2017**, *119*, 519–521. [CrossRef]
29. Kato, R.; Igarashi, S.; Umakoshi, T.; Verma, P. Tip-enhanced raman spectroscopy of multiwalled carbon nanotubes through d-band imaging: Implications for nanoscale analysis of interwall interactions. *ACS Appl. Nano Mater.* **2020**, *3*, 6001–6008. [CrossRef]
30. Wang, C.-B.; Deo, G.; Wachs, I.E. Interaction of polycrystalline silver with oxygen, water, carbon dioxide, ethylene, and methanol: In situ Raman and catalytic studies. *J. Phys. Chem. B* **1999**, *103*, 5645–5656. [CrossRef]
31. Tang, L.; Ji, R.; Cao, X.; Lin, J.; Jiang, H.; Li, X.; Teng, K.S.; Luk, C.M.; Zeng, S.; Hao, J. Deep ultraviolet photoluminescence of water-soluble self-passivated graphene quantum dots. *ACS Nano* **2012**, *6*, 5102–5110. [CrossRef]
32. Bai, Z.; Yu, D.; Wang, J.; Zou, Y.; Qian, W.; Fu, J.; Feng, S.; Xu, J.; You, L. Synthesis and photoluminescence properties of semiconductor nanowires. *Mater. Sci. Eng. B* **2000**, *72*, 117–120. [CrossRef]
33. Zhu, S.; Song, Y.; Wang, J.; Wan, H.; Zhang, Y.; Ning, Y.; Yang, B. Photoluminescence mechanism in graphene quantum dots: Quantum confinement effect and surface/edge state. *Nano Today* **2017**, *13*, 10–14. [CrossRef]
34. Kim, S.-H.; Ngo, H.H.; Shon, H.; Vigneswaran, S. Adsorption and photocatalysis kinetics of herbicide onto titanium oxide and powdered activated carbon. *Sep. Purif. Technol.* **2008**, *58*, 335–342. [CrossRef]

35. Chen, C.-Y.; Hsu, L.-J. Kinetic study of self-assembly of Ni (II)-doped TiO_2 nanocatalysts for the photodegradation of azo pollutants. *RSC Adv.* **2015**, *5*, 88266–88271. [CrossRef]
36. Kumar, K.V.; Porkodi, K.; Rocha, F. Langmuir–Hinshelwood kinetics–a theoretical study. *Catal. Commun.* **2008**, *9*, 82–84. [CrossRef]
37. Wang, H.; Wei, W.; Li, F.; Huang, B.; Dai, Y. Step-like band alignment and stacking-dependent band splitting in trilayer TMD heterostructures. *Phys. Chem. Chem. Phys.* **2018**, *20*, 25000–25008. [CrossRef]
38. Yakimov, A.; Dvurechenskii, A.; Nikiforov, A.; Bloshkin, A.; Nenashev, A.; Volodin, V. Electronic states in Ge/Si quantum dots with type-II band alignment initiated by space-charge spectroscopy. *Phys. Rev. B* **2006**, *73*, 115333. [CrossRef]
39. Wendisch, F.J.; Abazari, M.; Mahdavi, H.; Rey, M.; Vogel, N.; Musso, M.; Diwald, O.; Bourret, G.R. Morphology-graded silicon nanowire arrays via chemical etching: Engineering optical properties at the nanoscale and macroscale. *ACS Appl. Mater. Interfaces* **2020**, *12*, 13140–13147. [CrossRef]
40. Chen, C.-Y.; Wei, T.-C.; Hsiao, P.-H.; Hung, C.-H. Vanadium oxide as transparent carrier-selective layer in silicon hybrid solar cells promoting photovoltaic performances. *ACS Appl. Energy Mater.* **2019**, *2*, 4873–4881. [CrossRef]
41. Lan, J.; He, B.; Haw, C.; Gao, M.; Khan, I.; Zheng, R.; Guo, S.; Zhao, J.; Wang, Z.; Huang, S. Band engineering of ZnO/Si nanowire arrays in Z-scheme heterojunction for efficient dye photodegradation. *Appl. Surf. Sci.* **2020**, *529*, 147023. [CrossRef]
42. Tang, C.-H.; Chen, K.-Y.; Chen, C.-Y. Solution-processed ZnO/Si based heterostructures with enhanced photocatalytic performance. *New J. Chem.* **2018**, *42*, 13797–13802. [CrossRef]
43. Chen, C.-Y.; Hsiao, P.-H.; Wei, T.-C.; Chen, T.-C.; Tang, C.-H. Well incorporation of carbon nanodots with silicon nanowire arrays featuring excellent photocatalytic performances. *Phys. Chem. Chem. Phys.* **2017**, *19*, 11786–11792. [CrossRef] [PubMed]
44. Huang, Z.; Fang, H.; Zhu, J. Fabrication of silicon nanowire arrays with controlled diameter, length, and density. *Adv. Mater.* **2007**, *19*, 744–748. [CrossRef]